Nonlinear Phenomena in Multiferroic Nanocapacitors: Joule Heating and Electromechanical Effects

Yunseok Kim,[†,*] Amit Kumar,[†] Alexander Tselev,[†] Ivan I. Kravchenko,[†] Hee Han,[‡] Ionela Vrejoiu,[§] Woo Lee,[‡] Dietrich Hesse,[§] Marin Alexe,[§] Sergei V. Kalinin,[†,*] and Stephen Jesse[†]

[†]The Center for Nanophase Materials Sciences, Oak Ridge National Laboratory, Oak Ridge, Tennessee 37831, United States, [‡]Korea Research Institute of Standards and Science (KRISS), Daejeon 305-340, Korea, and [§]Max Planck Institute of Microstructure Physics, D-06120 Halle (Saale), Germany

ABSTRACT We demonstrate an approach for probing nonlinear electromechanical responses in $BiFeO_3$ thin film nanocapacitors using half-harmonic band excitation piezoresponse force microscopy (PFM). Nonlinear PFM images of nanocapacitor arrays show clearly visible clusters of capacitors associated with variations of local leakage current through the $BiFeO_3$ film. Strain spectroscopy measurements and finite element modeling point to significance of the Joule heating and show that the thermal effects caused by the Joule heating can provide nontrivial contributions to the nonlinear electromechanical responses in ferroic nanostructures. This approach can be further extended to unambiguous mapping of electrostatic signal contributions to PFM and related techniques.

KEYWORDS: multiferroic nanocapacitor · conduction · nonlinear response · Joule heating · PFM

Polarization switching in ferroelectric and multiferroic materials has been intensively investigated in the context of memory devices including ferroelectric-based data storage[1,2] and ferroelectric random access memories.[3,4] In parallel, conduction mechanisms in these materials have been explored both from the fundamental science and to explore the relationship between leakage currents and device reliability and degradation.[5−9] These studies have recently acquired new significance once the correlation between conduction and polarization state of the material was established, thus opening the pathway to applications such as ferroelectric tunneling barriers and domain wall conduction.[10−13]

Much of the progress in understanding domain- and domain-wall-mediated phenomena in ferroelectrics was made possible due to the emergence of local scanning probe microscopy (SPM) techniques. Piezoresponse force microscopy (PFM) has become a powerful method for imaging and control of polarization in ferroelectric thin films and device structures.[14−16] At the same time, conductive atomic force microscopy (CAFM) allows local *I*−*V* measurements and imaging of the resistance state of the surface. Using a combination of these techniques, Seidel *et al.* reported that conduction depends on the domain wall of multiferroic $BiFeO_3$ (BFO) thin films and manipulated current levels controlled by a number of conductive domain walls.[12,17−19] Several groups have explored tunneling conduction by polarization control in $Pb(Zr,Ti)O_3$ (PZT) thin films and also showed nondestructive recording based on the tunneling current reading.[13,20−22]

We note that a unique aspect of local studies by SPM is high local potential and current densities. Hence, in addition to physical mechanisms of interest such as bias-induced polarization switching and current flow, a broad spectrum of thermal and electromechanical effects can emerge. In particular, Joule heating induced by current flow may result in a number of effects, which can contribute to measured PFM signal. It also can result in a local increase of temperature, which facilitates the domain nucleation and growth. These effects are relevant for both SPM studies (*e.g.*, Joule heating contribution to measured electromechanical signal, temperature-induced changes in electromechanical coupling constants) and actual nanocapacitor structures (degradation, thermally assisted electrochemical processes, activation of switching) for high-density memory applications.[23,24] However, there is still a lack of information on the interplay between conduction and domain switching behavior, as well as a dearth of local methods that can establish the presence of local heating in materials and submicrometer structures.

Here, we explore the interplay between nonlinear electromechanical response, conduction currents, and Joule heating in model BFO thin film capacitor structures. These offer idealized model systems that can support large current densities and possess

* Address correspondence to kimy4@ornl.gov, sergei2@ornl.gov.

Received for review August 30, 2011 and accepted September 28, 2011.

Published online September 28, 2011
10.1021/nn203342v

well-defined geometry and uniform surface properties. We develop the approach based on half-harmonic band excitation for selectively probing the nonlinear responses associated with Joule heating effects and establish quantitative guidelines to predict the role of thermal effects.

RESULTS AND DISCUSSION

Linear and Nonlinear Electromechanical Responses in Ferroic Structures. PFM is by now established as the universal technique to visualize and probe ferroelectric domain structures and their switching behavior across multiple classes of ferroic material and devices.[16,25,26] In single-frequency PFM mode, the first-harmonic response of PFM is monitored to detect ferroelectric polarization, owing to the direct relationship between the deformation and bias, $d \sim d_{33}V_{ac}$. The theory of the PFM image formation mechanism for free ferroelectric surfaces and capacitor structures is by now well understood.[27−31]

However, we note that application of the periodic electric bias ($V_{ac} = V_0\sin(\omega t)$) to the material will result in response both at the modulation frequency and at its higher harmonics. In the thin film capacitor geometry, the first-harmonic response in the PFM has contributions due to piezoelectric and electrostatic interactions and, for a good tip−surface contact at low frequencies, can be represented as (see eq S9 in Supporting Information):

$$A_{PR,\omega} = \left(d + \frac{C_{cant}'}{k_{cant}}\right)V_0 \qquad (1)$$

where d, V_0, k_{cant}, and C_{cant} are the effective piezoelectric coefficient of the ferroelectric film, the amplitude of the driving bias, the spring constant of the cantilever, and the cantilever−sample capacitance, respectively.

At the same time, the capacitive, electrostrictive, and Joule heating effects are all quadratic in driving force and hence can be expected to contribute to the second-harmonic of cantilever response. By eq S14 in Supporting Information, the second-harmonic response in the PFM is expressed as

$$A_{PR,2\omega} = MV_0^2 + \beta\frac{RI_0^2}{2} + \frac{C_{cant}'}{4k_{cant}}V_0^2 \qquad (2)$$

where M, β, R, and I_0 are the effective electrostrictive coefficient, the Joule heat transduction coefficient (*i.e.*, a factor describing conversion of the Joule heat into mechanical displacement), the capacitor electrical resistance, and the amplitude of the capacitor current I_{ac}, respectively. Note that capacitive cantilever−surface interaction scales reciprocally with the stiffness of cantilever and is quadratic with applied bias. The electrostrictive and Joule heating contributions are virtually independent of elastic properties of the systems and are quadratic in voltage amplitude and capacitor current, respectively. We further note that, for situations when resistance R is significantly larger than the impedance of the voltage source, the driving bias V_{ac} can be maintained across the sample irrespectively of I_{ac} value.

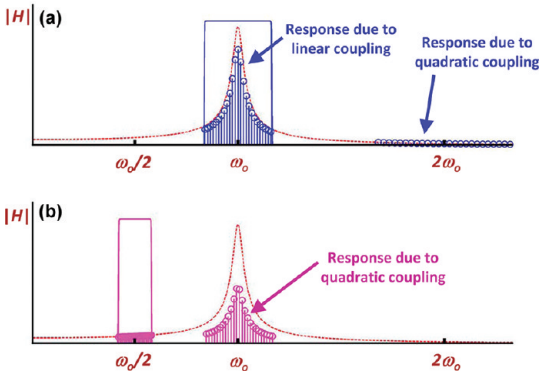

Figure 1. Operation principle of (a) first ω_0 and (b) half $\omega_0/2$ harmonic BE-PFM mode.

The structure of eq 2 suggests that identification of nonlinear interactions requires (a) reliable measurements of quadratic interactions obviating the topographic cross-talk and (b) establishing the origins of the contrast (voltage *vs* current driven). One approach for these measurements can be based on spectroscopic measurements in which signal *versus* V_{ac} is measured at each location on the sample surface.[32] However, these measurements require acquisition of high-dimensional data (3D for single frequency and 4D for band excitation (BE)) and also necessitate deconvolution of linear and quadratic terms.

Here, we develop an approach for probing quadratic interactions in PFM using the half-harmonic BE (HBE). As shown in Figure 1a, when the driving modulation bias V_{ac} with a band of frequencies with a central frequency at a cantilever resonant frequency ω_0 is applied to the sample for the BE method,[33] the conventional BE-PFM response can be obtained from the first-harmonic response at the same frequency due to the direct linear coupling of the bias. In addition, second-harmonic response with a band of frequencies is generated at the double frequency $2\omega_0$ due to the quadratic terms in eq 2 and generally falls outside of the cantilever resonance and detection band.

In this study, we excite the sample with an HBE signal at a frequency $\omega_0/2$, as shown in Figure 1b, to maximize the BE-PFM response at the resonant frequency ω_0. Therefore, the driving modulation bias with a band of frequencies at half-harmonic frequency $\omega_0/2$ is applied to the conductive probe, and its second-harmonic response is monitored over a band of frequencies around the resonant frequency ω_0. This approach extends an earlier work by Harnagea *et al.*, by allowing decoupling nonlinear interactions and topographic cross-talk.[34]

Nonlinear PFM Imaging of Capacitor Structures. Pt nanocapacitors with a diameter of around 380 nm were prepared using ultrathin anodic aluminum oxide (AAO) shadow masks on an epitaxial BFO (001) thin film with a thickness of 90 nm. The details of fabrication conditions of BFO thin films can be found in the Methods section.

Typical topography and leakage current maps of the capacitors are displayed in Figure 2a,d. Geometry of each capacitor is well-defined, as is seen in Figure 2a. The leakage current level of each capacitor can be clearly identified from the current maps in Figure 2d. The resistance level from the leakage current measurements is varying from kiloohms to gigaohms over the entire area of the sample. Individual capacitors show uniform leakage current levels over the entire area of each capacitor, as can be expected for a configuration with conductive top electrodes. The first-harmonic BE-PFM amplitude and phase images of Figure 2b,c show distribution of polarization amplitude and direction along the BFO film thickness. The as-prepared domain structure was clearly observed in different capacitors.[35] However, HBE-PFM amplitude and phase images in Figure 2e,f, respectively, show entirely new information, which is not associated with the as-prepared domain structures underneath the nanocapacitors. Some of the nanocapacitors in the HBE-PFM amplitude image in Figure 2e appear uniformly bright against a dark background.

To verify relationship between half- and first-harmonic BE responses, negative and positive poling procedures were performed on the capacitors. Under negative poling, there was observed a significant change of the domain structure (Figure 3a,c), whereas the HBE-PFM amplitude does not show any significant change (compare Figure 3b,d). This indicates that the HBE response is not directly related to the first-harmonic BE response, that is, polarization distribution in the material.

Nonlinear PFM *versus* Leakage Currents. As mentioned earlier (see eq 2), the second-harmonic response in the PFM includes capacitive, electrostrictive, and Joule heating contributions. In order to establish the origins of the HBE signal, we note that capacitive and electrostrictive interactions are expected to be approximately uniform across the sample surface and cannot explain the clear contrast and the formation of the capacitor clusters in the HBE amplitude images of Figures 2 and 3.

Figure 4 shows maps of topography, first-harmonic BE response, HBE response, resonant frequency, and current over the same region acquired within several subsequent scans. The HBE-PFM amplitude does not show any correlation with the first-harmonic BE-PFM response as well as with the resonant frequency. However, the clear contrast in the HBE-PFM amplitude image exactly corresponds to high leakage current, as is evident from Figure 4e,f.[36] This considerable correlation therefore suggests that it is the Joule heat generated by high leakage current flow through the nanocapacitors that primarily contributes to the second-harmonic response.

We further measured HBE nonlinearity curves on both weakly and highly leaky capacitors, as shown in Figure 5b. For weakly leaky capacitors, the capacitive and electrostrictive interactions mainly contribute to the second-harmonic response since Joule heating can be negligible in this case, whereas all three interactions contribute to the second-harmonic response of highly leaky capacitors. The highly leaky capacitors show a much higher HBE nonlinear response, which can be attributed to additional Joule heating.

To further clarify the heat generation in the high leakage current nanocapacitors, strain spectroscopy measurements were performed at the capacitors with two different leakage current levels.[13] In these, the local strain induced by application of dc to a SPM probe is measured directly through a static displacement of the SPM probe. As shown in Figure 5c, highly leaky capacitors of monodomain states exhibit higher strain amplitudes with more a symmetric shape of hysteresis loop. The difference in the strain loops is more significant for the multidomain nanocapacitors. For typical multidomain capacitors with low leakage currents, an asymmetric and/or incomplete switching can exist at the bias sweeps in the range between -5 and $+5$ V due to the domains stabilized by strain relaxation and partially due to built-in fields in the sample (Figure 5d).[37] Even though some of the weakly leaky capacitors show very asymmetric loops, highly leaky capacitors in the multidomain state always show more symmetric loops and higher average strain amplitudes. The higher amplitude characteristic of highly leaky capacitors in both mono- and multidomain states can originate from thermal expansion of BFO thin films due to Joule heating.[38] In turn, the more symmetric shape of the hysteresis loops can appear due to thermally assisted switching.[39,40] In fact, it is well-established that higher temperatures lead to smaller coercive voltages in ferroelectric films and accelerate their back-switching. Therefore, the measured local switching behavior depends on local thermal behavior and leakage current level. This is especially true for BFO thin films, which generally show higher leakage currents than typical ferroelectric materials such as PZT and $BaTiO_3$.[41] In this situation, the interplay between thermal and switching behavior of our BFO capacitors can be nontrivial to understand.

Analysis of Nonlinear Response. The strain spectroscopy measurements clearly show that the HBE response is associated with the high leakage current of the capacitors. With a harmonically oscillating bias voltage applied to a BFO capacitor $V_{ac} = V_0\sin(\omega t)$, where t is

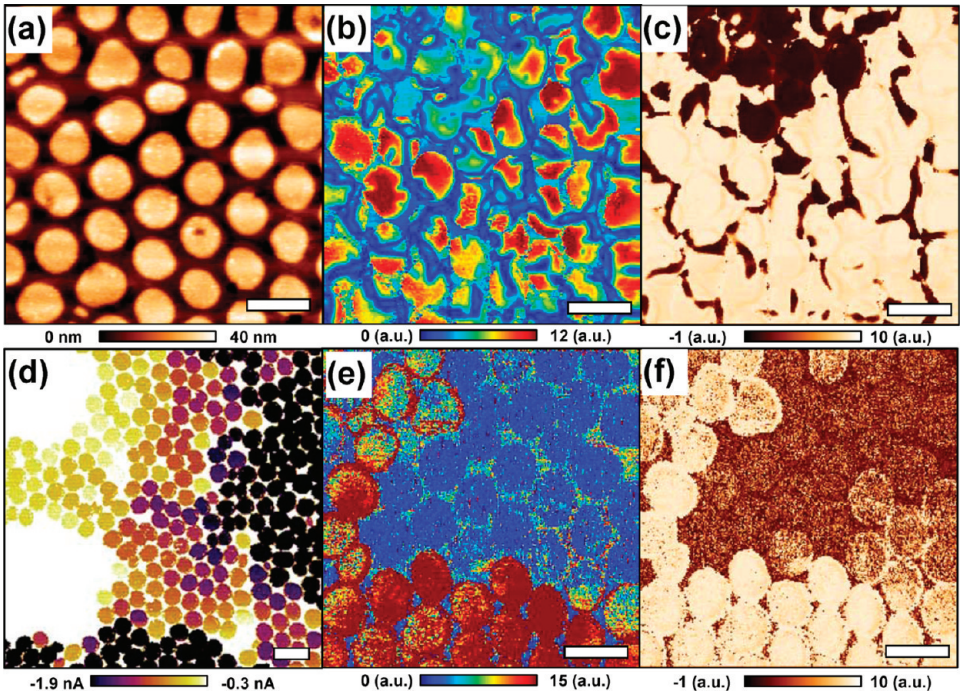

Figure 2. (a) Topography map, (d) current map, (b,e) amplitude and (c,f) phase images of first-harmonic BE-PFM (b,c) and HBE-PFM (e,f) of BFO nanocapacitors. All images except (d) were obtained from the same area. Scale bar is 560 nm.

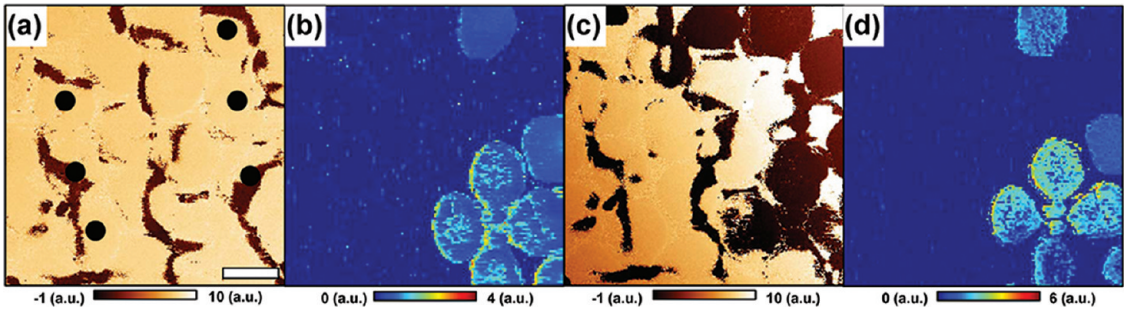

Figure 3. (a,c) PFM phase and (b,d) HBE-PFM amplitude images of BFO thin film nanocapacitors in (a,b) as-prepared states and in (c,d) as-poled states. Voltage biases of −3.5 V (+3.5 V) were applied to the right (left) three capacitors marked by black full circles in panel (a). Scale bar is 400 nm.

time and ω is an angular frequency, the power P dissipated in a leaky capacitor with a resistance R_{cap} is

$$P = I_{ac}^2 R_{cap} = \frac{V_{ac}^2}{R_{cap}} = \frac{V_0^2}{R_{cap}}\sin^2(\omega t)$$

$$= \frac{V_0^2}{2R_{cap}} - \frac{V_0^2}{2R_{cap}}\cos(2\omega t) = P_0 - P_{2\omega}\cos(2\omega t) \quad (3)$$

The second relation can be applied since the leaky capacitors in this study follow Ohm's law in the voltage range used in the experiments as can concluded from $I-V$ measurements of the capacitors (not shown). In the steady state, the displacement of the surface resulting from thermal expansion occurs only due to the oscillating part of the Joule power $P_{2\omega}$ with a frequency 2ω and an amplitude $\delta z_0 = \beta P_{2\omega}$, where β is the transduction coefficient referred to the power (see eq 2 and eq S12 in Supporting Information). The factor β depends on the frequency, materials properties in the vicinity of the capacitor, as well as on details of the heat generation and heat loss in the sample, such as distribution of Joule heat generation in the volume and heat exchange with the substrate and surrounding. Since the resistance of the Pt electrode is much smaller than the resistance of the BFO film, the variations of this factor β across the electrode will be responsible for the HBE image contrast in the case of a negligible tip−electrode contact resistance (so that the amplitude of the current I_0 remains constant).

It should be taken into consideration that other factors with the V_{ac}^2 dependence may contribute to the HBE signal. One of them can be thermal expansion of the cantilever tip pyramid due to Joule heat generated in the metallic coating of the tip itself or in the tip−surface junction due to the tip−Pt electrode contact resistance, which can be high in the case of a damaged

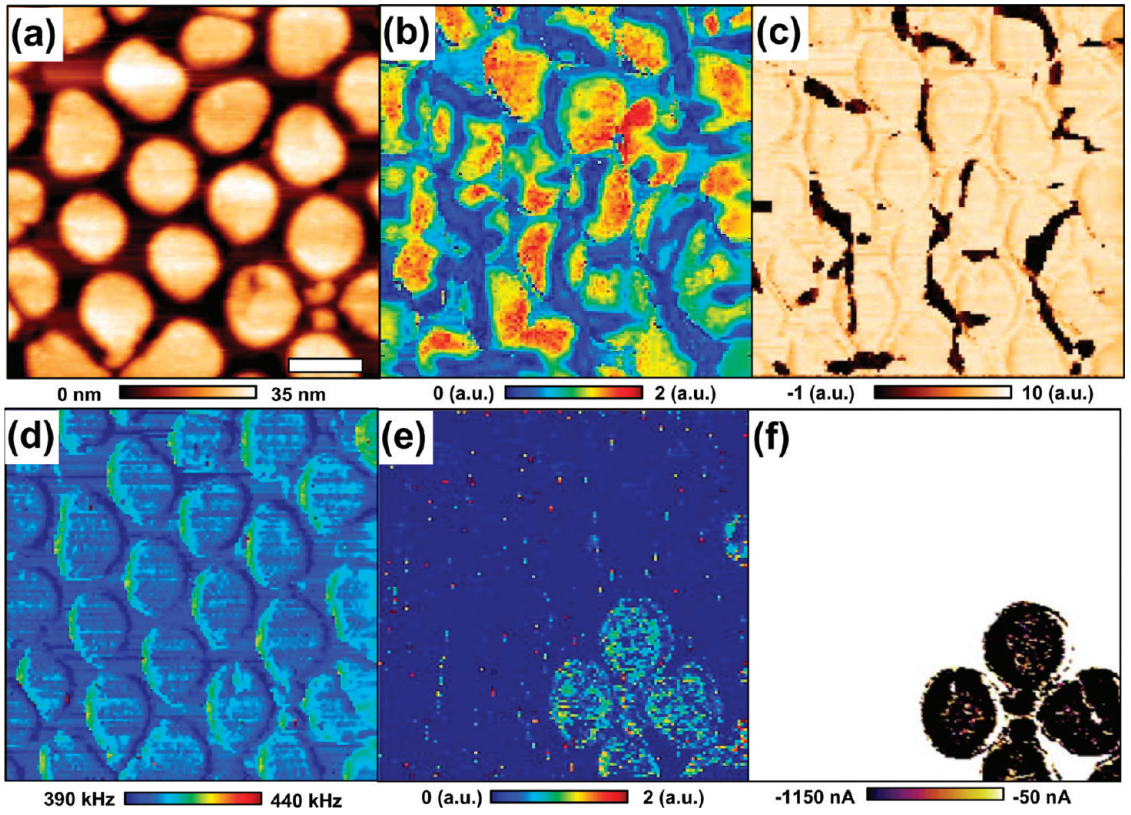

Figure 4. (a) Topography, (b,c) first-harmonic BE-PFM (b) amplitude and (c) phase, (d) resonant frequency, (e) HBE-PFM amplitude, and (f) current maps of BFO nanocapacitors obtained with a bias of −250 mV applied to the conductive SPM tip. Scale bar is 400 nm.

tip coating or a contaminated or rough electrode surface. The others are electrostriction and capacitance mentioned above (see eq 2). Our experiments showed that the former contribution can be significant in the HBE response, and special care should be taken to eliminate it from the data (a procedure for this is described in Supporting Information). The following analysis of the experimental data demonstrates that the procedure results in the elimination of the contribution from the tip expansion in the HBE signal.

Let us consider possible contribution of the tip expansion as an example. The periodic thermal expansion of the tip with a resistance R_{tip} can be accounted analogously to the expansion of the sample (Figure 5a). The microscope signal will be then proportional to the sum of the surface displacement and the tip expansion with a combined amplitude $\Delta z_0 = \delta z + \delta z_{tip}$:

$$\Delta z_0 = \frac{V_0^2}{2(R_{cap}+R_{tip})^2}(\beta_{cap}R_{cap} + \beta_{tip}R_{tip}) \approx \frac{V_0^2}{2R_{cap}}\left(\beta_{cap} + \beta_{tip}\frac{R_{tip}}{R_{cap}}\right) \quad (4)$$

Here, we used the fact that $R_{tip} \ll R_{cap}$. The values of Δz_0 obtained from HBE experiments can be plotted as functions of $V_0^2/(2R_{cap})$. As follows from eq 4, the data should fall on straight lines with slopes determined by the combination $(\beta_{cap} + \beta_{tip}R_{tip}/R_{cap})$, and they will be different for different R_{cap} values if the term $\beta_{tip}R_{tip}/R_{cap}$ accounting for the tip contribution is large. However, for a small contribution of the tip (*i.e.*, for $\beta_{cap} \gg \beta_{tip}R_{tip}/R_{cap}$), the data should follow the same straight line independently from the capacitor resistance. Figure 6 demonstrates that this is the case for our capacitors for the data processed according to the contact resistance elimination procedure mentioned above. Indeed, when the contact is good, there is no significant HBE signal for the tip contribution, which was verified with a 200 nm thick Pt film on a SiO_2/Si substrate as a sample and a variable resistor of 77−177 kΩ in series with the probe tip under the same experimental conditions as with the BFO nanocapacitors.

Numerical simulations further justified the experimental results. The coefficient β cannot be found analytically for the real sample geometry, and we used finite element (FE) analysis to directly calculate surface displacements resulting from the time-dependent part of the dissipated power. The FE modeling was performed using a COMSOL v4.2 multiphysics FE analysis package. Figure 6 displays the calculated amplitude δz_0 of the periodic displacements of the Pt electrode surface along the surface normal in the center of the

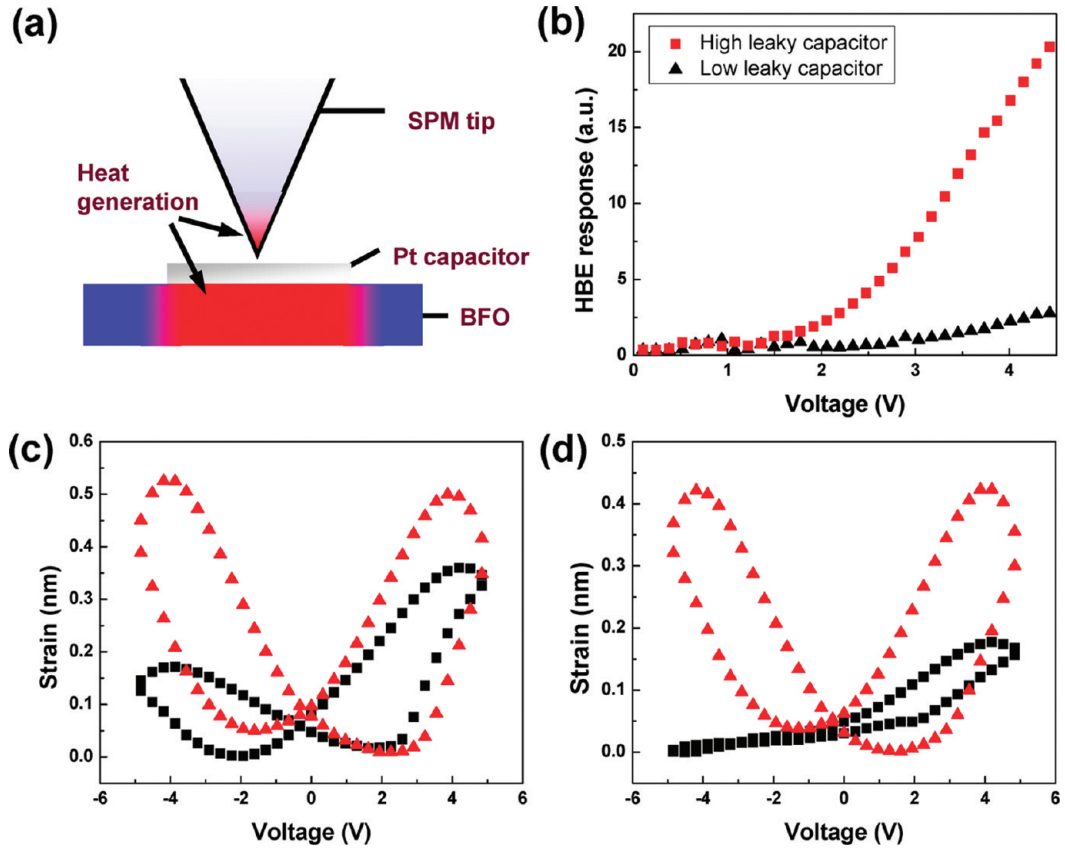

Figure 5. (a) Schematic of heat generation on the tip−electrode junction and the nanocapacitor structures. (b) HBE nonlinearity curves of weakly and highly leaky capacitors visible in Figure 4f. Strain loops of (c) mono- and (d) multidomain nanocapacitors with low (black square, $R > 1$ GΩ) and high (red triangle, $R \approx 40$ kΩ) leakage currents. Vertical offset was adjusted for each strain loop.

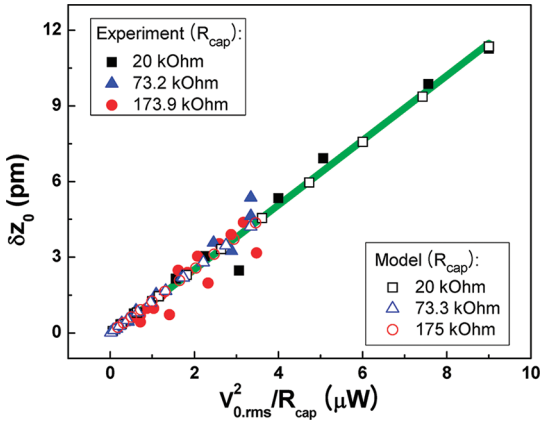

Figure 6. Amplitude δz_0 of the periodic displacements of the electrode surface along the surface normal in the center of the electrode as a function of the oscillating part of the dissipated Joule power for three capacitors with resistances R_{cap} = 20, 73.3, and 175 kΩ. Full symbols correspond to experimental points, open symbols are results of the numerical FE modeling, and the green solid line is a linear fit for all experimental data points.

electrode as a function of $P_{2\omega}$ together with the experimental data for three values of the capacitor resistance. As is seen, the results of the FE model and the experimental data are in excellent agreement. The peak-to-peak temperature swing in the electrode center was found to be about 8 °C for the lowest resistance of the capacitor with amplitude of the dissipated power of 9 μW.

SUMMARY

In summary, combining SPM experiments and numerical modeling, we have investigated the interplay between nonlinear electromechanical responses, conduction currents, and Joule heating in BFO nanocapacitors. We have developed a PFM technique based on half-harmonic excitations that allows selectively probing of nonlinear responses associated with Joule heating, electrostrictive, and capacitive effects. The clear contrast of clearly visible capacitor was observed in HBE amplitude. On the basis of the comparison between HBE amplitude and current maps, the HBE-PFM contrast can be explained by Joule heating generated by high leakage current through the BFO film. The strain spectroscopy measurements also show that a local increase of temperature due to Joule heating contributes to polarization switching along with the thermal expansion. The FE modeling indicates significance of the Joule heating contribution to the nonlinear response. The results show that the thermal effects due to Joule heating can provide nontrivial contributions to the electromechanical response,

which is relevant for both SPM studies and actual high-density memory applications, thus allowing improvements of SPM techniques as well as opening new pathways in the nanoscale memory applications.

We further note that the proposed strategy based on excitation of half-harmonic signals can be further extended to analysis of second-, third-, and higher harmonic signals obviating the (poorly understood) effects of cantilever transfer function. Hence, this approach is ideally suited for probing broad spectrum of nonlinear interactions in scanning probe microscopy.

METHODS

Materials. An epitaxial BFO thin film with a thickness of 90 nm was grown by pulsed laser deposition on a (001)-oriented 75 nm thick $SrRuO_3$ (SRO) bottom electrode deposited on a $SrTiO_3$ (STO) substrate. The details of the growth conditions of BFO thin films can be found elsewhere.[42] Ultrathin AAO shadow masks were prepared by anodization of aluminum[35,43,44] and placed on the BFO thin films. Then, 25 nm thick Pt top electrodes were deposited through the AAO shadow mask by electron beam evaporation. Finally, film-type Pt/BFO/SRO nanocapacitors with a diameter of around 380 nm were obtained by removing the AAO mask.

Measurements. Scanning probe microscopy studies were carried out with a commercial system (Asylum Cypher) additionally equipped with a Labview/Matlab-based BE controller and a current amplifier (Femto DLPCA-200). First-harmonic and HBE-PFM were performed at 340−460 kHz and 170−230 kHz, respectively, with 0.5 V_{pp} BE bias signal applied to a Pt/Cr-coated SPM probe (Budget Sensors Multi75E-G). Strain spectroscopy was performed at a bias sweep rate of 100 Hz. Using the strain spectroscopy, the local strain loops were directly acquired from a static displacement under an application of dc to the SPM probe. The detailed information in the HBE-PFM measurements can be found on the Supporting Information.

HBE Signal Calibration. The amplitude of the microscope photodetector signal V_ω^{ph} produced by a harmonic displacement $\delta z(t) = \delta z \sin(\omega t)$ of the sample surface in contact with the tip can be expressed as follows:

$$V_\omega^{ph} = sS_0(\omega)\delta z \tag{5}$$

where s is the detector sensitivity, that is, the conversion factor between the displacement of the tip and the photodetector output voltage, and $S_0(\omega)$ has a meaning of the frequency response (transfer) function of the cantilever. For the lowest resonant vibration mode (eigenmode) of the cantilever in contact with a sample, which is used in our BE experiments, the cantilever deformation is very close in shape to pure bending caused by a constant force applied to the tip apex. Therefore, it can be considered that $S_0(0) = 1$ for this mode, which is generally not the case for higher modes. The response of the cantilever to a small harmonic excitation with an angular frequency ω close to a frequency of a resonant mode ω_0 can be well-described as a response of a simple harmonic oscillator (SHO) with complex oscillation amplitude:[33,45]

$$H(\omega) = \frac{A{\omega_0}^2}{\omega^2 + i\frac{\omega\omega_0}{Q} - {\omega_0}^2} \tag{6}$$

where ω_0 is the eigenfrequency of the cantilever mode, Q is the quality factor of the mode, and A is directly proportional to the intensity (amplitude) of the driving excitation. It is easy to see that for the lowest mode $S_0(\omega) = H(\omega)/A$.

Factor s in eq 5 can be determined using standard procedures of the microscope calibration, for example, through analysis of force−distance curves.[46] To obtain values of δz, the amplitude of the microscope response V_ω^{ph} as a function of frequency is first fit by the functional form:

$$|H(\omega)| = \frac{A\omega_0^2}{\sqrt{(\omega^2 - \omega_0^2)^2 + (\omega\omega_0/Q)^2}} \tag{7}$$

with A, ω_0, and Q being fitting parameters, and then the displacement amplitude δz_0 is obtained using the calibrated detector sensitivity s and the value of the parameter A: $\delta z_0 = A/s$. Note, that $|H(\omega_0)| = AQ$, and with Q being close to 100−200, this determines the high sensitivity of the method to the small sample surface displacements down to subpicometer range. This calibration procedure is valid for both BE and HBE measurement modes.

Finite Element Analysis. The FE modeling was performed with a Joule heating and thermal expansion module of COMSOL v4.2 multiphysics FE analysis package. The model is 2D axisymmetric with actual thickness and radius of the capacitor electrode as well as BFO and SRO film thicknesses. The model layout is shown in Figure S1 of the Supporting Information. The harmonically oscillating bias voltage was applied between the SRO/STO interface and the upper surface of the Pt electrode. The material properties used in the model are listed in Table S-I of the Supporting Information. The conductivity of the BFO film was adjusted to results in the resistance of the capacitor matching the experimental values. Since the displacement of the sample surface is increasing with the volume of the material affected by the Joule heating, the overall size of the model should be sufficiently large. Here we used the fact that the periodic surface displacements occur due to periodic temperature modulations in a limited volume of the sample. Indeed, the lateral size of the sample volume involved in the periodic thermal expansion and contraction is about of the thermal penetration depth for the frequency 2ω: $l_T = (\alpha_T/2\omega)^{1/2}$, where $\alpha_T = k/(\rho C_p)$ is the thermal diffusivity, k is the thermal conductivity, ρ is density, and C_p is the material specific heat.[47] For the parameters for STO given in Table S-I, $l_T \approx 1.5$ μm for a frequency $\omega/(2\pi) = 170$ kHz used in the experiments. The radius and height of the FE model were set to 10 μm $\gg l_T$, and the temperature at the outer boundaries of the model was set to a constant value of 20 °C. The calculations were performed with a time-dependent solver starting from an initial condition of zero current and a uniform temperature across the sample equal to 20 °C until the steady state is apparently reached (after about five periods of the bias voltage oscillations).

Acknowledgment. This research was conducted at the Center for Nanophase Materials Sciences, which is sponsored at Oak Ridge National Laboratory by the Office of Basic Energy Sciences, U.S. Department of Energy.

Supporting Information Available: Derivations of equations for the first- and second-harmonic PFM response, FE model layout and materials properties used in the FE model, as well as a procedure for elimination of contact resistance contribution in the HBE-PFM measurements. This material is available free of charge *via* the Internet at http://pubs.acs.org.

REFERENCES AND NOTES

1. Ahn, C. H.; Tybell, T.; Antognazza, L.; Char, K.; Hammond, R. H.; Beasley, M. R.; Fischer, Ø.; Triscone, J.-M. Local, Nonvolatile Electronic Writing of Epitaxial $Pb(Zr_{0.52}Ti_{0.48})O_3$/$SrRuO_3$ Heterostructures. *Science* **1997**, *276*, 1100–1103.

2. Tanaka, K.; Kurihashi, Y.; Uda, T.; Daimon, Y.; Odagawa, N.; Hirose, R.; Hiranaga, Y.; Cho, Y. Scanning Nonlinear Dielectric Microscopy Nano-Science and Technology for Next Generation High Density Ferroelectric Data Storage. *Jpn. J. Appl. Phys.* **2008**, *47*, 3311–3325.
3. Scott, J. F. *Ferroelectric Memories*; Springer: Heidelberg, 2000.
4. Waser, R.; Bottger, U.; Tiedke, S. *Polar Oxides: Properties, Characterization and Imaging*; John Wiley & Sons Inc.: New York, 2004.
5. Stolichnov, I.; Tagantsev, A. Space-Charge Influenced-Injection Model for Conduction in $Pb(Zr_xTi_{1-x})O_3$ Thin Films. *J. Appl. Phys.* **1998**, *84*, 3216.
6. Stolichnov, I.; Tagantsev, A.; Setter, N.; Cross, J. S.; Tsukada, M. Control of Leakage Conduction of High-Fatigue-Endurance $(Pb,La)(Zr,Ti)O_3$ Film Ferroelectric Capacitors with $Pt/SrRuO_3$ Electrodes. *Appl. Phys. Lett.* **1999**, *75*, 1790.
7. Baniecki, J. D.; Cross, J. S.; Tsukada, M.; Watanabe, J. H_2O Vapor-Induced Leakage Degradation of $Pb(Zr,Ti)O_3$ Thin-Film Capacitors with Pt and IrO_2 Electrodes. *Appl. Phys. Lett.* **2002**, *81*, 3837.
8. Baniecki, J. D.; Shioga, T.; Kurihara, K.; Kamehara, N. Investigation of the Importance of Interface and Bulk Limited Transport Mechanisms on the Leakage Current of High Dielectric Constant Thin Film Capacitors. *J. Appl. Phys.* **2003**, *94*, 6741.
9. Meyer, R.; Liedtke, R.; Waser, R. Oxygen Vacancy Migration and Time-Dependent Leakage Current Behavior of $Ba_{0.3}Sr_{0.7}TiO_3$ Thin Films. *Appl. Phys. Lett.* **2005**, *86*, 112904.
10. Blom, P. W. M.; Wolf, R. M.; Cillessen, J. F. M.; Krijin, M. P. C. M. Ferroelectric Schottky Diode. *Phys. Rev. Lett.* **1994**, *73*, 2107–2110.
11. Kohlstedt, H.; Pertsev, N. A.; Rodríguez Contreras, J.; Waser, R. Theoretical Current−Voltage Characteristics of Ferroelectric Tunnel Junctions. *Phys. Rev. B* **2005**, *72*, 125341.
12. Seidel, J.; Martin, L. W.; He, Q.; Zhan, Q.; Chu, Y.-H.; Rother, A.; Hawkridge, M. E.; Maksymovych, P.; Yu, P.; Gajek, M.; *et al.* Conduction at Domain Walls in Oxide Multiferroics. *Nat. Mater.* **2009**, *8*, 229–234.
13. Maksymovych, P.; Jesse, S.; Yu, P.; Ramesh, R.; Baddorf, A. P.; Kalinin, S. V. Polarization Control of Electron Tunneling into Ferroelectric Surfaces. *Science* **2009**, *324*, 1421–1425.
14. Alexe, M.; Harnagea, C.; Hesse, D.; Gösele, U. Patterning and Switching of Nanosize Ferroelectric Memory Cells. *Appl. Phys. Lett.* **1999**, *75*, 1793.
15. Bdikin, I. K.; Shvartsman, V. V.; Kholkin, A. L. Nanoscale Domains and Local Piezoelectric Hysteresis in $Pb(Zn_{1/3}Nb_{2/3})O_3$-4.5%$PbTiO_3$ Single Crystals. *Appl. Phys. Lett.* **2003**, *83*, 4232.
16. Gruverman, A.; Kholkin, A. Nanoscale Ferroelectrics: Processing, Characterization and Future Trends. *Rep. Prog. Phys.* **2006**, *69*, 2443.
17. Seidel, J.; Maksymovych, P.; Batra, Y.; Katan, A.; Yang, S.-Y.; He, Q.; Baddorf, A. P.; Kalinin, S. V.; Yang, C.-H.; Yang, J.-C.; *et al.* Domain Wall Conductivity in La-Doped $BiFeO_3$. *Phys. Rev. Lett.* **2010**, *105*, 197603.
18. Maksymovych, P.; Seidel, J.; Chu, Y. H.; Wu, P.; Baddorf, A. P.; Chen, L.-Q.; Kalinin, S. V.; Ramesh, R. Dynamic Conductivity of Ferroelectric Domain Walls in $BiFeO_3$. *Nano Lett.* **2011**, *11*, 1906–1912.
19. Farokhipoor, S.; Noheda, B. Conduction through 71o Domain Walls in $BiFeO_3$ Thin Films. DOI: arXiv:1104.3267v1.
20. Gruverman, A.; Wu, D.; Lu, H.; Wang, Y.; Jang, H. W.; Folkman, C. M.; Zhuravlev, M. Ye.; Felker, D.; Rzchowski, M.; Eom, C.-B.; *et al.* Tunneling Electroresistance Effect in Ferroelectric Tunnel Junctions at the Nanoscale. *Nano Lett.* **2009**, *9*, 3539–3543.
21. Garcia, V.; Bibes, M.; Bocher, L.; Valencia, S.; Kronast, F.; Crassous, A.; Moya, X.; Enouz-Vedrenne, S.; Gloter, A.; Imhoff, D.; *et al.* Ferroelectric Control of Spin Polarization. *Science* **2010**, *327*, 1106–1110.
22. Pantel, D.; Goetze, S.; Hesse, D.; Alexe, M. Room-Temperature Ferroelectric Resistive Switching in Ultrathin $Pb(Zr_{0.2}Ti_{0.8})O_3$ Films. *ACS Nano* **2011**, *5*, 6032–6038.
23. Yu, H. Y.; Li, M.-F.; Kwong, D.-L. Thermally Robust HfN Metal as a Promising Gate Electrode for Advanced MOS Device Applications. *IEEE Trans. Electron Devices* **2004**, *51*, 609–615.
24. Jiang, Q. Y.; Subbarao, E. C.; Cross, L. E. Effect of Composition and Temperature on Electric Fatigue of La-Doped Lead Zirconate Titanate Ceramics. *J. Appl. Phys.* **1994**, *75*, 7433.
25. Kalinin, S. V.; Shao, R.; Bonnell, D. A. Local Phenomena in Oxides by Advanced Scanning Probe Microscopy. *J. Am. Ceram. Soc.* **2005**, *88*, 1077–1098.
26. Balke, N.; Bdikin, I.; Kalinin, S. V.; Kholkin, A. L. Electromechanical Imaging and Spectroscopy of Ferroelectric and Piezoelectric Materials: State of the Art and Prospects for the Future. *J. Am. Ceram. Soc.* **2009**, *92*, 1629–1647.
27. Morozovska, A. N.; Eliseev, E. A.; Kalinin, S. V. The Piezoresponse Force Microscopy of Surface Layers and Thin Films: Effective Response and Resolution Function. *J. Appl. Phys.* **2007**, *102*, 074105.
28. Morozovska, A. N.; Eliseev, E. A.; Bravina, S. L.; Kalinin, S. V. Resolution-Function Theory in Piezoresponse Force Microscopy: Wall Imaging, Spectroscopy, and Lateral Resolution. *Phys. Rev. B* **2007**, *75*, 174109.
29. Scrymgeour, D. A.; Gopalan, V. Nanoscale Piezoelectric Response across a Single Antiparallel Ferroelectric Domain Wall. *Phys. Rev. B* **2005**, *72*, 024103.
30. Guyonnet, J.; Béa, H.; Guy, F.; Gariglio, S.; Fusil, S.; Bouzehouane, K.; Triscone, J.-M.; Paruch, P. Shear Effects in Lateral Piezoresponse Force Microscopy at 180° Ferroelectric Domain Walls. *Appl. Phys. Lett.* **2009**, *95*, 132902.
31. Agronin, A.; Molotskii, M.; Rosenwaks, Y.; Strassburg, E.; Boag, A.; Mutchnik, S.; Rosenman, G. Nanoscale Piezoelectric Coefficient Measurements in Ionic Conducting Ferroelectrics. *J. Appl. Phys.* **2005**, *97*, 084312.
32. Bintachitt, P.; Jesse, S.; Damjanovic, D.; Han, Y.; Reaney, I. M.; Trolier-McKinstry, S.; Kalinin, S. V. Collective Dynamics Underpins Rayleigh Behavior in Disordered Polycrystalline Ferroelectrics. *Proc. Natl. Acad. Sci. U.S.A.* **2010**, *107*, 7219–7224.
33. Jesse, S.; Kalinin, S. V.; Proksch, R.; Baddorf, A. P.; Rodriguez, B. J. The Band Excitation Method in Scanning Probe Microscopy for Rapid Mapping of Energy Dissipation on the Nanoscale. *Nanotechnology* **2007**, *18*, 435503.
34. Harnagea, C.; Pignolet, A.; Alexe, M.; Hesse, D. High-Order Electromechanical Response of Thin Films by Contact Resonance Piezoresponse Force Microscopy. *IEEE Trans. Ultrason., Ferroelectr., Frequency Control* **2006**, *53*, 2309–2322.
35. Kim, Y.; Han, H.; Rodriguez, B. J.; Vrejoiu, I.; Lee, W.; Baik, S.; Hesse, D.; Alexe, M. Individual Switching of Film-Based Nanoscale Epitaxial Ferroelectric Capacitors. *J. Appl. Phys.* **2010**, *108*, 042005.
36. Note that leakage current of some BFO nanocapacitors in Figure 3 was slightly changed after various switching experiments.
37. Kim, Y.; Kumar, A.; Ovchinnikov, O.; Jesse, S.; Han, H.; Pantel, D.; Vrejoiu, I.; Lee, W.; Hesse, D.; Alexe, M.; *et al.* Unpublished.
38. Wang, D.; Fotinich, Y.; Carman, G. P. Influence of Temperature on the Electromechanical and Fatigue Behavior of Piezoelectric Ceramics. *J. Appl. Phys.* **1998**, *83*, 5342.
39. Yuan, G. L.; Liu, J.-M.; Zhnag, S. T.; Wu, D.; Wang, Y. P.; Liu, Z. G.; Chan, H. L. W.; Choy, C. L. Low-Temperature Switching Fatigue Behavior of Ferroelectric $SrBi_2Ta_2O_9$ Thin Films. *Appl. Phys. Lett.* **2004**, *84*, 954.
40. Yimnirun, R.; Wongmaneerung, R.; Wongsaenmai, S.; Ngamjarurojana, A.; Ananta, S.; Laosiritaworn, Y. Temperature Scaling of Dynamic Hysteresis in Soft Lead Zirconate Titanate Bulk Ceramic. *Appl. Phys. Lett.* **2007**, *90*, 112906.
41. Pabst, G. W.; Martin, L. W.; Chu, Y.-H.; Ramesh, R. Leakage Mechanisms in $BiFeO_3$ Thin Films. *Appl. Phys. Lett.* **2007**, *90*, 072902.
42. Kim, Y.; Vrejoiu, I.; Hesse, D.; Alexe, M. Reversible Plasma Switching in Epitaxial $BiFeO_3$ Thin Films. *Appl. Phys. Lett.* **2010**, *96*, 202902.
43. Lee, W.; Han, H.; Lotnyk, A.; Schubert, M. A.; Senz, S.; Alexe, M.; Hesse, D.; Baik, S.; Göesele, U. Individually Addressable Epitaxial Ferroelectric Nanocapacitor Arrays with near Tb $inch^{-2}$ Density. *Nat. Nanotechnol.* **2008**, *3*, 402–407.

44. Kim, Y.; Han, H.; Lee, W.; Baik, S.; Hesse, D.; Alexe, M. Non-Kolmogorov–Avrami–Ishibashi Switching Dynamics in Nanoscale Ferroelectric Capacitors. *Nano Lett.* **2010**, *10*, 1266–1270.
45. Albrecht, T. R.; Grütter, P.; Horne, D.; Rugar, D. Frequency Modulation Detection Using High-Q Cantilevers for Enhanced Force Microscope Sensitivity. *J. Appl. Phys.* **1991**, *69*, 668.
46. Harnagea, C.; Pignolet, A.; Alexe, M.; Hesse, D.; Göesele, U. Quantitative Ferroelectric Characterization of Single Submicron Grains in Bi-Layered Perovskite Thin Films. *Appl. Phys. A: Mater. Sci. Process.* **2000**, *70*, 261–267.
47. Cahill, D. G. Thermal Conductivity Measurement from 30 to 750 K: The 3ω Method. *Rev. Sci. Instrum.* **1990**, *61*, 802.